A Novel Approach for the Classification of Liver MR Images Using Complex Orthogonal Ripplet-II and Wavelet-Based Transforms

Ayşe Elif Canbilen and Murat Ceylan

Abstract This study presents a decision support system aid to radiologists for defining focal lesions and making diagnosis more accurate by using liver magnetic resonance images. A new method called the complex orthogonal Ripplet-II transform is proposed as a feature extraction procedure. Artificial neural network is utilized to classify the obtained features as a hemangioma or cyst. The results are evaluated with the results of the systems using Ridgelet, Ripplet type-II and orthogonal Ripplet type-II transforms. The highest accuracy ratio (85.3%) and area under curve value (0.92) are achived by the complex orthogonal Ripplet-II transform. The accuracy of the classification procedure is increased up to 95.6% by a combined system that collectively analyzes the results obtained from the artificial neural network outputs of the two methods (Ridgelet and complex orthogonal Ripplet-II transforms). While this combined system is built up of three methods (adding Ripplet type-II), the accuracy rate reaches 97.06% and the area under curve value to 0.99.

Keywords Artificial neural network · Biomedical image classification
Complex orthogonal Ripplet-II transform · Complex wavelet transform
Liver MR imaging · Ripplet type-II transform

1 Introduction

Liver is an important organ in human body which has several vital tasks, such as synthesizing protein, producing biochemicals necessary for digestion and regulating blood glucose [25]. Hence, any disease occurring to the liver needs to be detected at

A.E. Canbilen (✉) · M. Ceylan
Department of Electrical and Electronics Engineering, Faculty of Engineering,
Selcuk University, 42075 Konya, Turkey
e-mail: ayseelif@selcuk.edu.tr

M. Ceylan
e-mail: mceylan@selcuk.edu.tr

N. Dey et al. (eds.), *Classification in BioApps*, Lecture Notes in Computational Vision and Biomechanics 26, https://doi.org/10.1007/978-3-319-65981-7_2

the earliest opportunity. A frequent liver abnormality is “lesion”, which is mostly benign. While cyst, hemangioma, focal nodular hyperplasia and hepatocellular adenoma are benign lesions, the most frequent malign lesions are hepatocarcinoma, cholangiocarcinoma and metastases [17]. The patients who have benign lesions need no treatment. On the other hand, if there are malign primer or metastatic lesions, surgical intervention and a specific treatment plan must be applied. So, the detection of a lesion and a definitive diagnosis are important points when planning a patient’s treatment. In addition to that, protection of patients with benign lesions from unnecessary intervention is just as important as defining malign masses sufficiently early.

The imaging methods used for defining liver lesions are computed tomography (CT), magnetic resonance (MR), spiral CT, angiography and so on. Among these diagnostic procedures, MR imaging is a significant method that ensures detailed screening of the tissues and organs. MR has the ability to discriminate between tissues according to their physicochemical characteristics. A significant correlation between the severity of liver diseases and progress of fibrosis is revealed by researchers. For instance, a fat ratio in the liver over a certain value is associated with hepatoma; a thin-walled structure containing liquid shows cysts and clustered thin-walled blood vessels indicate hemangioma [27]. The liver lesions are determined and qualified by taking advantage of the signal differences of T1 and T2 weighted dynamic contrast MR. The contrasting material sensitivity of lesions in various stages aids in making a definitive diagnosis. While it is possible to make a qualitative analysis with this process, quantitative values cannot be attained. The diagnosis accuracy rate of these kinds of qualitative evaluation by radiologists cannot exceed 72% [26, 27].

Pixel density values give quantitative information about the content of images. The local differences between pixel values make MR images definable and meaningful. The computation region of the image contrast should be compatible with the organ size. However, it is impossible to define an optimal resolution value in that the screened images have varied sizes. Moreover, details of different resolution images contain diversified information. In order to overcome this problem, multi-resolution analysis (MRA) methods have been efficiently utilized for image analysis since the improvement of Wavelet transform (WT) which is also applied on biomedical images [16, 19]. Real valued WT can be applied on images only in horizontal, vertical, and diagonal directions. So, WT is inadequate for the detection of discontinuities in other angles and expressing two-dimensional (2D) singularities. Therefore, there is a need to develop different procedures and enhance the performance of existing methods. A complex form of discrete WT is proposed and a study to eliminate the disadvantages of real valued WT regarding direction is introduced [12, 24]. The limited direction problem of WT is resolved by the development of the Ridgelet transform (RT) [4]. RT, which uses angular windows, detects one-dimensional (1D) discontinuities in images via constant ridgelets along the lines, and has been effectively used in image analysis [6, 8]. A complex form of RT is applied for denoising [7]. However, it is necessary to develop the RT to identify 2D discontinuities such as curves. The Ripplet type-II transform (Rip-II)

and orthogonal Ripplet type-II transform (OrtRip-II) are developed as scalable and shiftable methods [30]. They are applicable in different directions at multiple levels. Rip-II has also gained a complex form and is used for classifying liver MR images such as hemangiomas or cysts [31]. It has been proved that the imaginary coefficients could achieve better results than the real ones. Thus, OrtRipp-II could also need to have a more complex form to increase its classification success.

There is a large body of research which uses different methods to classify liver lesions [2, 11, 13, 14, 17, 23]. In these studies, attempts were made to classify lesions as normal, cirrhosis, fatty, cyst, hemangioma, malignancy, hepatitis, carcinoma, benign and metastases. Accuracy rates of 92 and 95% were achieved in classification applications in [14, 16], respectively. Area under curve (AUC) values are obtained between 0.87 and 0.97 using different classification methods to estimate the degree of liver fibrosis [10]. The performances of different techniques were compared for the classification of malignant liver tumors and found AUC values at a maximum of 0.89 [15]. In another study for the identification and classification of liver focal lesions, AUC = 0.95 was obtained [9]. The process time was shortened with a study of classifying liver MR images as either a hemangioma or cyst to compare the performances of artificial neural network (ANN) and an extreme learning machine [1]. Four different phases for each liver MR image were combined and the benign/malign masses were classified with an accuracy rate of 90% [18]. Fatty liver disease is detected with an accuracy rate of 97.58% [21].

The main goal of this study is to propose a decision support system for defining focal lesions and making diagnosis more accurate by obtaining computational values from liver MR images. Dynamic contrast-enhanced liver MR (1.5 T) images, obtained from Selcuk University Faculty of Medicine Department of Radiology, are used for the application. Four MRA methods are utilized for feature extraction. Three of these methods are already presented in the literature: RT, Rip-II and OrtRip-II. The fourth method, complex OrtRip-II, which is applied in more directions in comparison to existing methods, is introduced by the authors of this study for the first time. ANN models are used for the classification process. The performance of the suggested systems is analyzed using specificity, sensitivity, accuracy and the AUC value of receiver operating characteristic (ROC) curves.

Classification in Bio-Applications: The classification of medical images has a key role in accurate diagnosis. However, qualitative evaluations by radiologists provide inadequate information from which to make a decision about abnormalities. Advances in computer aided diagnosis (CAD) systems have ensured a considerable increase in the accuracy rates of medical image interpretation. In this context, this chapter on the classification of liver MR images presents a decision support system aid to radiologists for the defining of focal lesions which uses an original method called complex OrtRipp-II and ANNs. Hemangioma and cyst lesions are successfully detected with an accuracy of 95.6%. This chapter is closely related to the special issue scope and the topics of this book on medical image processing, classification techniques, machine learning, biomedical applications, CAD systems and neural networks for classification.

2 Methods

The methods used in the application procedure are examined in five sections. The segmentation procedure is explained in Sect. 2.1; feature extraction methods are analyzed in detail in Sects. 2.2 and 2.3; and the method used in the classification stage is explained in Sect. 2.4. Finally, the performance evaluation procedures are described in Sect. 2.5.

2.1 Segmentation

Image segmentation is carried out to divide pixels into meaningful and interpretable image sections (such as objects or parts of the object). Segmentation of the liver from MR images to distinguish the masses is an important preliminary procedure for feature extraction applications in that the images contain redundant details which do not contribute to characterizing the lesions. These unnecessary areas cause misevaluation of the mathematical methods which try to interpret the lesions by using the pixel values. Thus, the methods should be applied only to the relevant parts of an MR image to obtain accurate results. Any error in segmentation continues incrementally in the subsequent steps. The redundant areas of the MR images in this study are eliminated by the segmentation procedure of the radiologists. An original liver MR image and its segmented version are seen in Fig. 1.

2.2 Multi-resolution Analysis (MRA) Methods for Feature Extraction

Radon and generalized Radon transforms that are the basis of Rip-II types (Rip-II, OrtRip-II and complex OrtRip-II) are given in Sect. 2.2.1. Rip-II transforms are explained in Sects. 2.2.2–2.2.5.

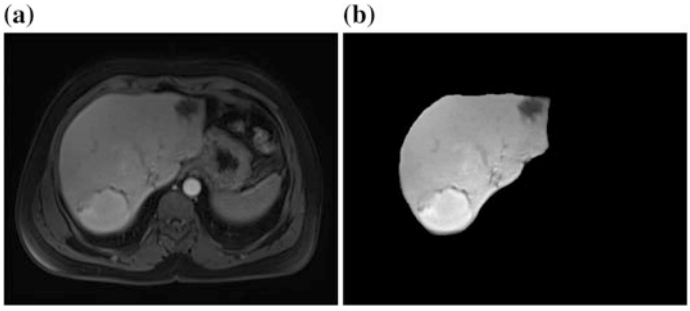

Fig. 1 **a** Original liver MR image, **b** Segmented version

2.2.1 Radon Transform (RAT) and Generalized Radon Transform (GRAT)

RAT makes curves in images into point discontinuities. The RAT of an image expressed as $f(x, y)$ is calculated from Eq. (1), while δ represents the Dirac distribution, r and θ refer to the constant radius and angular values, respectively.

$$P(r, \theta) = \int_{R^2} f(x, y)\, \delta(x \cos\theta + y \sin\theta - r)\, \mathrm{d}x\mathrm{d}y \tag{1}$$

The generalized RAT (GRAT) is obtained by the expansion of RAT in such a way as to be applicable along a family of curves. While the RT is based on RAT, Rip-II methods are mainly based on GRAT [29, 30].

Curves can be defined in polar coordinates (ρ, ϕ), as shown in Eq. (2):

$$\rho^{1/d} \cos\left(\frac{1}{d}(\phi - \theta)\right) = r^{1/d} \tag{2}$$

where d refers to the degree. In addition, the d values should be selected as $|d| \geq 1$ while defining the curves for the Rip-II.

GRAT is calculated from Eq. (3) in polar coordinates [30]. The function should first be defined in (ρ, ϕ) space to calculate the GRAT of 2D and the real valued $f(x, y)$ function.

$$\mathrm{GRAT}\,(r, \theta) = \int_0^{2\pi} \int_r^{\infty} \rho f(\rho, \phi)\, \delta(r - \rho \cos^d((\phi - \theta)/d))\, \mathrm{d}\rho\mathrm{d}\phi \tag{3}$$

GRAT can also be calculated by using the Fourier transform (FT). Both forward and inverse Fourier functions are defined, respectively, for a $f(\rho, \phi)$ function defined in polar coordinate in Eqs. (4) and (5):

$$f_n(\rho) = \int_0^{2\pi} f(\rho, \phi) e^{-in\phi}\, \mathrm{d}\phi \tag{4}$$

$$f(\rho, \phi) = \frac{1}{\pi} \sum_{n=-\infty}^{\infty} f_n(\rho) e^{in\phi} \tag{5}$$

GRAT can be denoted as shown in Eq. (6). While the $f_n(\rho)$ function is the FT of $f(\rho, \phi)$, the $g_n(r)$ expression is defined by using the $T_n(.)$ Chebyshev polynomial from the nth order for $d > 0$ [30].

$$\mathrm{GRAT}\,(r,\theta) = \sum_{n=-\infty}^{\infty} g_n(r)\, e^{in\theta} \tag{6}$$

The GRAT pair is expressed as shown in Eqs. (7) and (8):

$$\begin{aligned}\mathrm{GRAT}(r,\theta) = 2\sum_{n=-\infty}^{\infty}\Bigg[\int_{r}^{\infty}\int_{0}^{2\pi} f(\rho,\phi)e^{-in\phi}\,\mathrm{d}\phi\,.\left(1-(r/\rho)^{2/d}\right)^{-1/2} \\ .T_n((r/p)^{1/d})\,\mathrm{d}\rho\Bigg]e^{in\theta}\end{aligned} \tag{7}$$

$$\begin{aligned}f(\rho,\phi) = -\frac{1}{\pi}\sum_{n=-\infty}^{\infty}\Bigg[\frac{\mathrm{d}}{\mathrm{d}\rho}\int_{\rho}^{\infty}\int_{0}^{2\pi}\mathrm{GRAT}(r,\theta)\,e^{-in\theta} \\ \cdot T_n((r/\rho)^{1/d}).((r/\rho)^{2/d}-1)^{-1/2}\frac{1/d}{r}\,\mathrm{d}\theta\mathrm{d}r\Bigg].e^{in\phi}\end{aligned} \tag{8}$$

2.2.2 Ridgelet Transform (RT)

RT is an MRA method that is calculated by wavelets in the Radon domain. The 2D Ridgelet function is defined in order to apply this transform where $\psi(.)$ is 1D Wavelet and $\boldsymbol{k} = (k_1, k_2) \in R^2$, as shown in Eq. (9). In addition, $a > 0$ is scale, $b \in R$ is shift and $\theta \in [0, 2\pi)$ is the direction parameter [29].

$$\psi_{a,b,\theta}(\boldsymbol{k}) = a^{-1/2}\,\psi[(k_1\cos\theta + k_2\sin\theta - b)/a] \tag{9}$$

Thus, the RT for a 2D function can be stated as shown in Eq. (10):

$$R(a,b,\theta) = \int_{R^2}\psi_{a,b,\theta}(\boldsymbol{k})f(k_1,k_2)\,\mathrm{d}k_1\mathrm{d}k_2 \tag{10}$$

The RT of a 2D $f(x,y)$ function, while $P(r,\theta)$ denotes RAT, could be mathematically given as shown in Eq. (11):

$$R(a,b,\theta) = \int_{R^2}\psi_{a,b}(r)\,P(r,\theta)\,\mathrm{d}r \tag{11}$$

where $\psi_{a,b}(r)$ is 1D WT, which is equal to the expression given in Eq. (12):

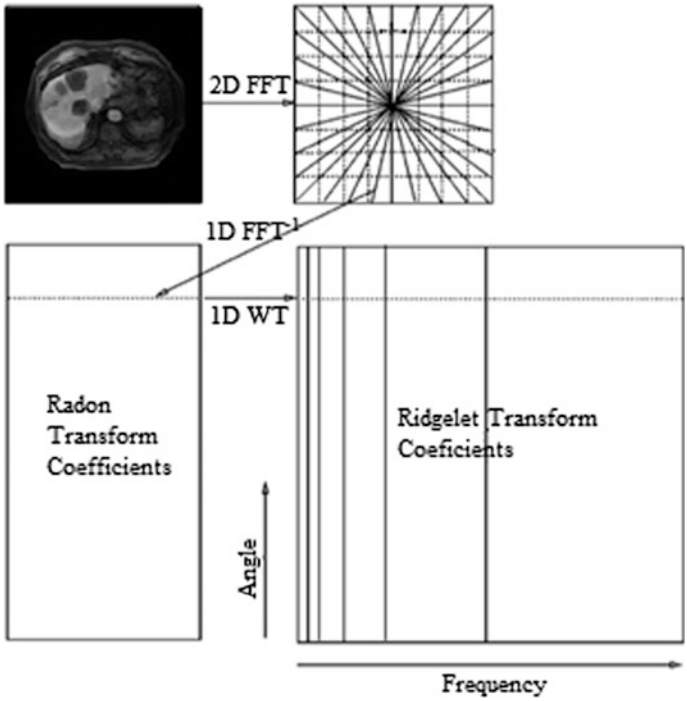

Fig. 2 Scheme of RT

$$\psi_{a,b}(r) = a^{-1/2}\psi(r-b)/a \tag{12}$$

It is clear that the RT is equal to the application of 1D WT to the slices of RAT. The operation scheme for the RT is given in Fig. 2.

2.2.3 Ripplet Type-II Transform (Ripp-II)

The Ripplet Type-II function $(\psi_{a,b,d,\theta}(\rho,\phi))$ at polar coordinates was defined to be used in the Rip-II (Eq. 13) [30]. This function includes a degree parameter $(d \in N)$ as well as scale $(a > 0)$, shift $(b \in R)$ and angle/direction $(\theta \in [0, 2\pi))$ parameters. Thus, it is scalable, shiftable and can be applied in different directions at multiple levels.

$$\psi_{a,b,d,\theta}(\rho,\phi) = a^{-1/2}\,\varphi((\rho\cos^d((\theta-\phi)/d) - b)/a) \tag{13}$$

The Rip-II of a 2D $f(\rho,\phi)$ function defined in polar coordinates is calculated by the inner product of the $f(\rho,\phi)$ function with the Rip-II function where $\bar{\psi}$ is the complex conjugate of ψ (Eq. 13):

$$R_f(a,b,d,\theta) = \int_0^{2\pi} \int_r^{\infty} \bar{\psi}_{a,b,d,\theta}(\rho,\phi) f(\rho,\phi)\, \rho \mathrm{d}\rho \mathrm{d}\phi \tag{14}$$

If the expression $\psi_{a,b,d,\theta}(\rho,\phi)$ in Eq. (14) is written as in Eq. (13) and then Eq. (14) is reorganized, the statement as shown in Eq. (15) is obtained:

$$\begin{aligned} R_f(a,b,d,\theta) = & \int_{\rho}^{\infty} a^{-1/2} \bar{\varphi}((r-b)/a) \\ & \cdot \left[\int_0^{2\pi} \int_r^{\infty} \delta(r - \rho \cos^d((\theta-\phi)/d)) f(\rho,\phi)\, \rho \mathrm{d}\rho \mathrm{d}\phi \right] \mathrm{d}r \end{aligned} \tag{15}$$

A detailed analysis of Eq. (15) shows that the Rip-II is equal to the inner product of GRAT and the 1D Wavelet. A liver MR image and Rip-II coefficients of this image are presented in Fig. 3. The coefficient matrix consists of approximation and detail components, and the information about the image is contained within the approximation component. So, this part is enough to identify the image and is used for the classification procedure.

The Rip-II can be inversed, as can all image analysis methods that are used in image processing. If we want to reobtain a known 2D $f(\rho,\phi)$ original signal from the Rip-II coefficients $(R_f(a,b,d,\theta))$, a 1D inverse WT is applied on the $R_f(a,b,d,\theta)$ coefficients and the inverse GRAT of the obtained result is then calculated. The inverse Rip-II can be mathematically denoted as shown in Eq. (16) [30]:

$$\begin{aligned} f(\rho,\phi) = -\frac{1}{\pi} \sum_{n=-\infty}^{\infty} & \left[\frac{\mathrm{d}}{\mathrm{d}\rho} \int_0^{2\pi} \int_{\rho}^{\infty} \int_{-\infty}^{\infty} \int_0^{\infty} \frac{1}{\sqrt{a}} R_f(a,b,d,\theta)\, \varphi\left(\frac{r-a}{b}\right) e^{-in\theta} \right. \\ & \left. \cdot T_{nd}((r/\rho)^{1/d})((r/\rho)^{2/d} - 1)^{-1/2} \frac{1/d}{r} \mathrm{d}a\mathrm{d}b\mathrm{d}r\mathrm{d}\theta \right] \cdot e^{in\phi} \end{aligned} \tag{16}$$

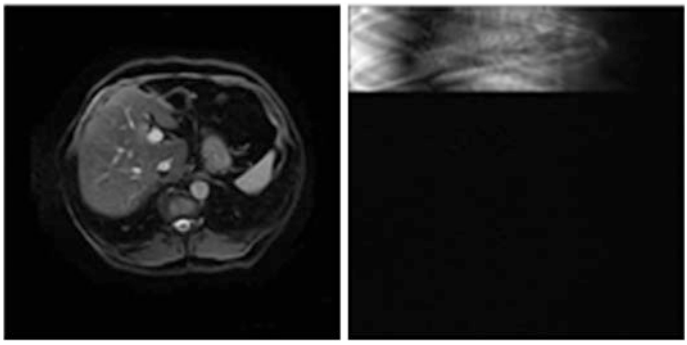

Fig. 3 A liver MR image (left) and Rip-II (d = 3, level = 2) coefficients (right) of this image

Rip-II is orientation invariant. In other words, the Rip-II coefficients of an image and a transformed version of this image at a particular angle are almost the same [30].

2.2.4 Orthogonal Ripplet Type-II Transform (OrtRipp-II)

The Orthogonal Ripplet type-II transform (OrtRip-II) contains similar operations to the Rip-II. The only difference in OrtRip-II is that a 2D WT is applied instead of a 1D WT after GRAT in Rip-II. Eq. (17) yields OrtRip-II coefficients of a 2D $f(\rho, \phi)$ function in a polar coordinate [30].

In OrtRip-II, information regarding the direction cannot be clearly obtained as WT is applied on both the r and θ parameters. More organized and sparse transform coefficients are obtained than Rip-II [30].

$$R_f^{ort}(a, b_1, b_2, d) = 2 \sum_{n=-\infty}^{\infty} \int_0^{2\pi} \int_{\rho}^{\infty} \frac{1}{a} \bar{\varphi}\left(\frac{r - b_1}{a}\right) \bar{\varphi}\left(\frac{\theta - b_2}{a}\right) \cdot \int_r^{\infty} \int_0^{2\pi} f(\rho, \phi) e^{-in\phi} \mathrm{d}\phi (1 - (r/\rho)^{2/d})^{-1/2} T_{nd}((r/\rho)^{1/d}) \mathrm{d}\rho e^{in\theta} \mathrm{d}r \mathrm{d}\theta \tag{17}$$

OrtRip-II can also be inverted. If 2D inverse WT and inverse GRAT are sequentially applied to $R_f^{ort}(a, b_1, b_2, d)$ transform coefficients appropriately, the original function $f(\rho, \phi)$ is obtained.

2.2.5 Complex Orthogonal Ripplet-II Transform (Complex OrtRip-II)

Successful results have been obtained in many image processing applications using real valued 2D WT [3, 28]. However, real WT has three main disadvantages [5]: (1) Even a small shift in input signal significantly changes Wavelet coefficients. This makes establishing a correlation between the slightly shifted signal and the original signal difficult. (2) It can be applied only in three directions (horizontal, vertical, diagonal). (3) It does not contain phase information, which is important for many image processing applications. A dual-tree complex WT was defined to eliminate these disadvantages of WT [24]. In this transform, coefficients are calculated in parallel operations as real and imaginary. A complex Wavelet $(\psi_{cplx}(\rho, \phi))$ used in these operations can be expressed as shown in Eq. (18), while $\psi_{re}(\rho, \phi)$ represents the real and $\psi_{im}(\rho, \phi)$ the imaginary part:

$$\psi_{cplx}(\rho,\phi) = (\psi_{re}(\rho,\phi) + j.\psi_{im}(\rho,\phi)) \tag{18}$$

While detail components are calculated in three directions $(0°, 45°, 90°)$ for real value 2D WT, they can be calculated in six different angles $(\pm 15°, \pm 45°, \pm 75°)$ both for the real and imaginary parts of the coefficients using a 2D dual-tree WT by the nature of the filter banks [22]. Thus, the phase information is protected and the shift invariant characteristic is achieved by performing operations in more directions.

A Wavelet set, consisting of six complex Wavelets in polar coordinates, to represent the directions as $i = 1, 2, 3$ can be formed by using Eqs. (19) and (20) for real parts and Eqs. (21) and (22) for the imaginary parts:

$$\psi_{re,\,i}(\rho,\phi) = \frac{1}{\sqrt{2}}\left(\psi_{1,\,i}(\rho,\phi) - \psi_{2,\,i}(\rho,\phi)\right) \tag{19}$$

$$\psi_{re,\,i+3}(\rho,\phi) = \frac{1}{\sqrt{2}}\left(\psi_{1,\,i}(\rho,\phi) + \psi_{2,\,i}(\rho,\phi)\right) \tag{20}$$

$$\psi_{im,\,i}(\rho,\phi) = \frac{1}{\sqrt{2}}\left(\psi_{3,\,i}(\rho,\phi) + \psi_{4,\,i}(\rho,\phi)\right) \tag{21}$$

$$\psi_{im,\,i+3}(\rho,\phi) = \frac{1}{\sqrt{2}}\left(\psi_{3,\,i}(\rho,\phi) - \psi_{4,\,i}(\rho,\phi)\right) \tag{22}$$

The complex OrtRip-II is developed using a 2D dual-tree complex WT to enhance the success of the OrtRip-II analysis. Moreover, it achieves the phase information and gains a shift invariant character. The fact that a greater number of superior results were obtained from the complex versions of the MRA methods than the real forms (Wavelet, Ridgelet and Curvelet) also suggested the necessity of a complex form for the Rip-II [32]. Thus, complex OrtRip-II has been developed as a new MRA technique.

The operation steps for the complex OrtRip-II are as follows:

- Express 2D $f(x, y)$ function given in a Cartesian coordinate as $f(\rho, \phi)$ in polar coordinates.
- Apply GRAT to $f(\rho, \phi)$ function using FT and Chebyshev polynomial.
- Apply 2D dual-tree complex WT to GRAT coefficients.
- Represent the transform coefficients as complex numbers by combining the real and imaginary sections of the obtained results.

Complex OrtRip-II could be mathematically defined as shown in Eq. (23):

$$R_f^{cplx}(a,b_1,b_2,d) = 2\sum_{n=-\infty}^{\infty}\int_0^{2\pi}\int_{\rho}^{\infty}\frac{1}{a}\bar{\varphi}_{cplx}\left(\frac{r-b_1}{a}\right)\bar{\varphi}_{cplx}\left(\frac{\theta-b_2}{a}\right)$$
$$\int_r^{\infty}\int_0^{2\pi} f(\rho,\phi).e^{-in\phi}\mathrm{d}\phi.(1-(r/\rho)^{2/d})^{-1/2}T_n((r/\rho)^{1/d})\,\mathrm{d}\rho.e^{in\theta}\mathrm{d}r\mathrm{d}\theta \tag{23}$$

A 2D $f(\rho,\phi)$ function with known complex OrtRip-II coefficients could be attained by inverse operations by using transform coefficients. First, the inverse 2D dual-tree complex WT should be applied to the obtained complex coefficients. Then, if inverse GRAT operation is applied to the result of the process, the $f(\rho,\phi)$ function can be obtained.

The scheme of the complex OrtRip-II is presented in Fig. 4. A liver MR image and second level complex OrtRip-II coefficients (coarse to finest) for $d = 2$ of this image are given in Fig. 5. As the coefficients are in complex form, those presented in Fig. 5 are the magnitude values of the coefficients.

The advantages and disadvantages of RT, Rip-II, OrtRip-II and complex OrtRip-II are presented in Table 1. It is understood from Table 1, that the complex OrtRip-II is superior to the other three methods. The complex OrtRip-II, which combined the high performance of the Rip-II in identification of 2D singularities along random shaped curves and a high direction provided by the complex wavelets, has the potential to obtain better results than the RT, Rip-II and OrtRip-II.

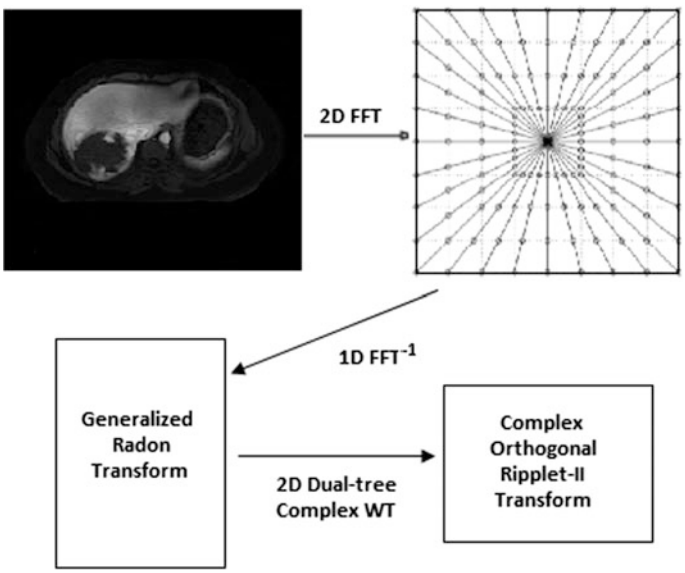

Fig. 4 Scheme of complex OrtRip-II

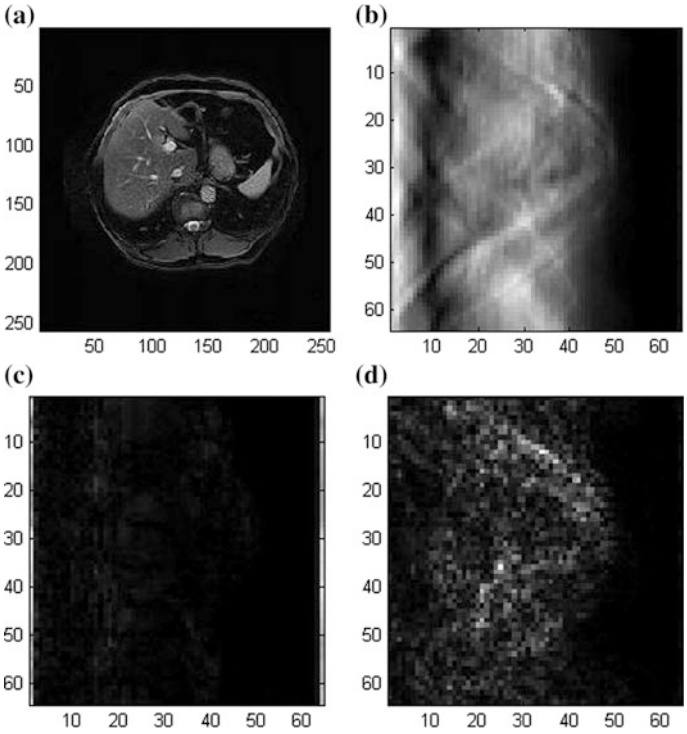

Fig. 5 **a** A liver MR image, **b–d** 2nd level complex OrtRip-II coefficients for $d = 2$ (**b**: Approximation, **c–d**: 2 of 6 detail components)

Table 1 Comparison of RT, Rip-II, OrtRip-II and complex OrtRip-II

	Advantages	Disadvantages
RT	–Successful in capturing 1D discontinuities	–Inadequate in 2D discontinuities
Rip-II	–Orientation invariant –Direction information can be clearly obtained	–Irregular coefficients
OrtRip-II	–More regular coefficients than Rip-II	–Direction information cannot be clearly obtained
Complex OrtRip-II	–Shift invariant –Contains phase information –Analysis in higher number of directions is possible	–Has more operation steps than other methods

2.3 Statistical Feature Extraction

Arithmetic mean, skewness, standard deviation, kurtosis and moment values of the approximation components of the transform coefficients are calculated for each transform in the feature extraction operation of our biomedical image classification application.

For a number sequence k, while n is the number of elements, the arithmetic mean is calculated from Eq. (24); and the standard deviation is calculated from Eq. (25).

$$\bar{k} = \frac{1}{n}\sum_{i=1}^{n} k_i = \frac{k_1 + k_2 + \ldots + k_n}{n} \tag{24}$$

$$\sigma = \sqrt{\frac{1}{n}\sum_{i=1}^{n} (k_i - \bar{k})^2} \tag{25}$$

The lth moment of a data set, with μ mean value, is calculated as shown in Eq. (26):

$$m_l = E(k - \mu)^l \tag{26}$$

Skewness and kurtosis are statistical measurements of the asymmetry status of data around the mean value. While σ is the standard deviation and $E(.)$ represents estimated value, skewness is calculated from Eq. (27) and kurtosis is calculated from Eq. (28).

$$s = \frac{E\left[(k - \mu)^3\right]}{\sigma^3} \tag{27}$$

$$q = \frac{E\left[(k - \mu)^4\right]}{\sigma^4} \tag{28}$$

2.4 Artificial Neural Network (ANN)

ANN structure is modeled by the communication mechanism between the human neural system and neurons. The signals come to neurons, are gathered in a center and transposed to other cells after processing the required information in the human neural system. ANN also produces a response which is key to the target values similar to the consecutive parallel operated reaction procedure of the brain. Inputs are multiplied by certain weights called neurons and attempts are made to try to approximate them to target values by using threshold values and activation

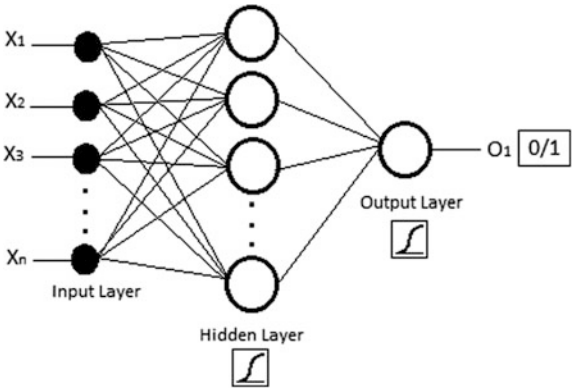

Fig. 6 ANN model used to classify liver images

functions. This operation is optimized for different problems by organizing the neuron numbers in layers and having various parameters specific to ANN. It is possible to create varied ANN structures according to the characteristics of the problem. The ANN model used for the classification operation in this study is presented in Fig. 6.

2.5 *Performance Evaluation Methods*

Various methods have been developed to evaluate the performance of classification applications. The image classification performances of the designed systems are compared by calculating the accuracy, specificity and sensitivity values of the results obtained using RT, Rip-II, OrtRip-II and complex OrtRip-II in this study.

Among the images that are known to be correctly labelled as cysts by the radiologists at system output are true positives (*TrP*); those that were labelled as hemangioma, however, which were evaluated as cysts, are false positives (*FaP*); those that were labelled as hemangioma, and were found as hemangioma are true negatives (*TrN*) and the images that were labelled as cysts, however, which were found to be hemangioma by the system are false negatives (*FaN*). The accuracy, sensitivity and specificity values are calculated from Eqs. (29), (30) and (31), respectively.

$$sen = \frac{TrP}{TrP + FaN} \tag{29}$$

$$spe = \frac{TrN}{FaP + TrN} \tag{30}$$

$$acc = \frac{TrP + TrN}{TrP + FaN + FaP + TrN} \tag{31}$$

The ROC curve is also used to compare the performances of the proposed methods. The ROC curve is drawn using *TrP* and *FaP* rates, and the AUC provides information about the sensitivity of the system. The AUC takes values between 0 and 1. AUC = 1 is an ideal system situation. Thus, the systems with an AUC value closer to 1 yield more accurate classification results.

3 Experiments

The proposed decision support system is a three-stage operation: segmentation, feature extraction and classification. Dynamic contrast-enhanced liver MR (1.5 T) images obtained from Selcuk University Faculty of Medicine Department of Radiology are used for the application. One slice which clearly shows the abnormality is chosen for each liver MR image.

In the first stage, slices of 68 liver MR images (28 hemangioma, 40 cyst) clearly indicate the lesions chosen for each patient by the radiologists according to biopsy reports. Moreover, the images are segmented by them to eliminate unnecessary details on the MR images. Then, the dimensions of the images are adjusted to 256×256.

In the second stage, four MRA methods (RT, Rip-II, OrtRip-II and complex OrtRip-II) are utilized to obtain the liver MR image features. The decomposition level chosen is 2 for all transforms to have objective results. In addition, statistical methods are used to reduce the size of the data.

Finally, after the preprocessing phase, the MR images are classified using an ANN model. The classification procedure is planned in three different ways: single ANN system, dual-combined system and triple-combined system.

3.1 Single ANN System

In this method, the classification procedure is applied by using a single ANN. The pipeline for the classification of liver MR images with single ANN is presented in Fig. 7 and the operation steps are:

- Segment the original MR images in such a way as to contain the liver only.
- Apply RT to all 68 liver MR images that are segmented with a fixed dimension of 256×256 and obtain transform coefficients.
- Calculate the mean, standard deviation, skewness, kurtosis and moment for each image using approximation components of the transform coefficients.
- Combine the calculated statistical values under a single feature vector for each image. Obtain 68 feature vectors.
- Enter the feature vectors you obtained as input to the ANN.

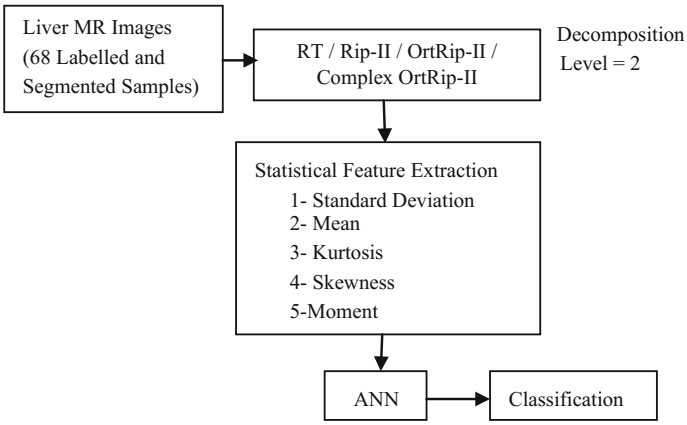

Fig. 7 The pipeline for the classification of liver MR images with a single ANN

- Adjust the target of the images labelled as hemangioma "0" and adjust the target of the images labelled as cyst "1" in the ANN. Classify the images as hemangioma or cyst according to the value obtained from the ANN output.

  if out < 0.5
  then out = hemangioma
  else out = cyst

  - Repeat steps 3–6 using Rip-II.
  - Repeat steps 3–6 using OrtRip-II.
  - Repeat steps 3–6 with the imaginary components and magnitude values of coefficients for complex OrtRip-II.

The logarithmic sigmoid function defined in the 0.1 range is used as the activation function in the ANN structure. The weights are renewed by calculating the difference (error) between the value obtained from the ANN output and target. The appropriate iteration number for the ANN model used in this study is determined as 150. The neuron number in the hidden layer and the rate of learning are found empirically as 30 and 0.7, respectively. The operations are performed by the leave-one-out cross validation method that individually tests each image.

Liver MR images are classified with an accuracy of 76.74% using Ridgelet; 67.65% using Rip-II; 61.76% using OrtRip-II; 83.82% using imaginary components, and with an accuracy of 85.3% using magnitude values of complex OrtRip-II. Considering this, it can be said that the best feature detection method for classification is complex OrtRip-II. Real and imaginary components of its coefficients yield results with the same accuracy.

3.2 Dual-Combined System

In this system, the classification results of two different single ANN systems are evaluated by logical operations. The purpose is to obtain a high-performance method by combining the results accurately classified only in one of the single ANN systems with the results correctly classified only in the other. The target is defined as "0" for hemangioma. Hence, the appropriate logical operation for hemangioma is "AND", in that it gives the dual-combined system result 0 when one of the chosen single ANN system results is 0. Similarly, "OR" operation is appropriate for cyst-labelled images because it yields the result 1 if one of the inputs is 1. The accuracy tables of AND and OR operations are given in Table 2.

The best results can be obtained with this system provided that:

- The first chosen method for the system should be the one which gives the maximum accuracy ratio. Hence, the number of images that have the possibility of being classified as inaccurate is minimized before interpreting the ANN results of the two methods together.
- The images which were counted in the wrong class with the first chosen method should be classified as accurate with the second method as much as possible.

The best pair for the dual-combined system is detected as the RT and complex OrtRip-II (with magnitude components). An accuracy rate of 95.6% is obtained with these methods (Fig. 8).

3.3 Triple-Combined System

A triple-combined system similar to the dual-combined system is also designed in this study (Fig. 9). Rip-II and OrtRip-II methods are incorporated into the dual-combined system, respectively. Thus, three ANN results are evaluated with the AND/OR procedures together. The triple-combined system has given the same results with Rip-II and OrtRip-II. It increases the accuracy rate to 97.06% and the AUC to 0.99.

Table 2 Accuracy tables of AND and OR operations

Inp-1	Inp-2	AND	OR
0	0	0	0
0	1	0	1
1	0	0	1
1	1	1	1

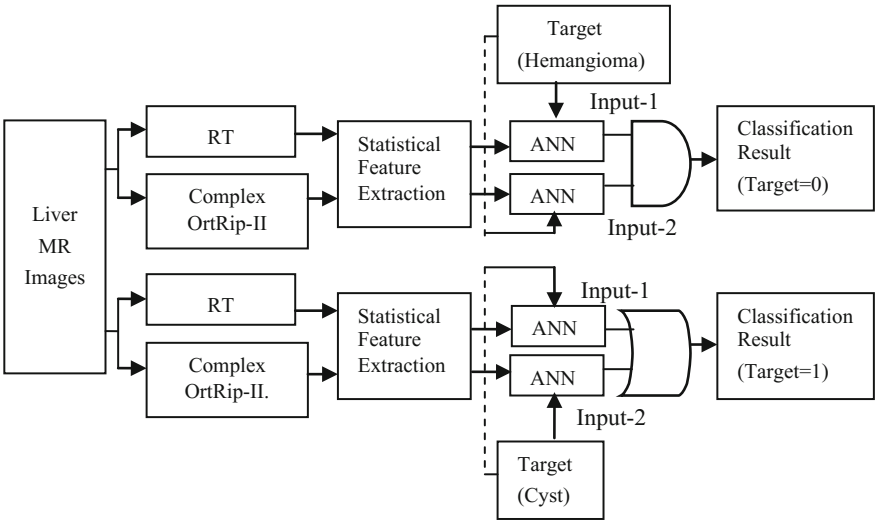

Fig. 8 Scheme of dual-combined system

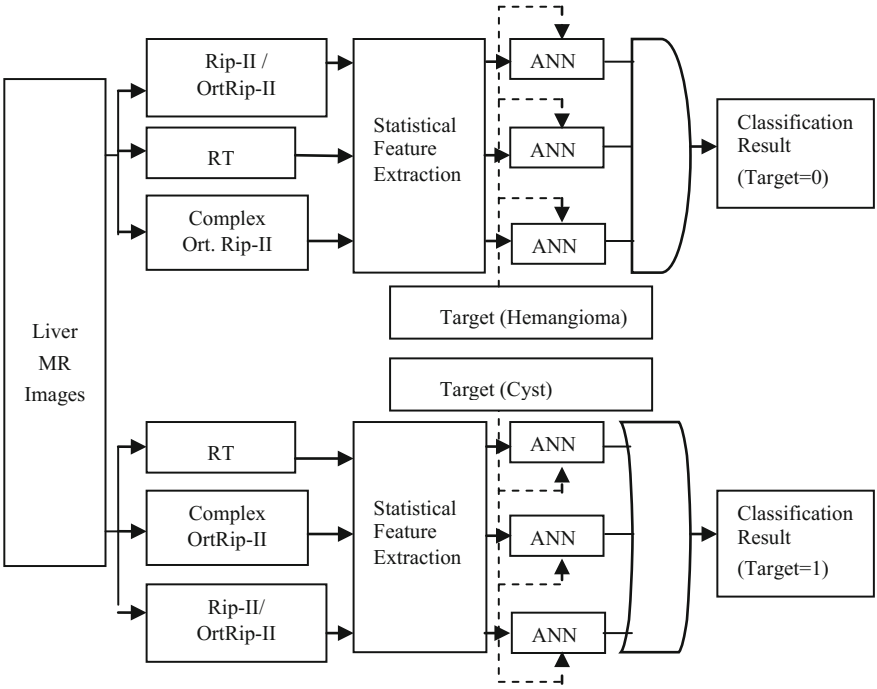

Fig. 9 Scheme of triple-combined system

4 Discussion and Results

Sensitivity, specificity and accuracy values are calculated in order to compare the performances of the systems. The obtained values are presented in Table 3. It could be understood from this table that the complex method suggested in this chapter gives optimum results among Rip-II types. This is also confirmed by comparing specificity, sensitivity and AUC values.

According to Table 3, the best system for classifying the liver MR images is the triple combined system and the most successful MRA method is the proposed complex OrtRip-II. The results of the classification carried out with the real/imaginary components and magnitude values of the complex OrtRip-II coefficients are almost the same.

In order to see how close the ANN outputs are to the target values for the hemangioma and cyst images, see the graphs in Fig. 10. It is understood that the triple-combined system gives the closest values to the target values for both classes (hemangioma, cyst).

Accuracy values obtained from previous research on the classification of liver symptoms are presented in Table 4. It is clearly seen that the highest accuracy value belongs to our study. Furthermore, the proposed combined models give higher AUC values than the studies which used AUC as the evaluation criteria [9, 10, 15]. The proposed triple-combined system gives the best results because the advantages of three MRA techniques are assembled in one algorithm.

The performances of the systems are compared by drawing ROC curves and calculating AUC values. ROC curves drawn for RT, Rip-II types (with real,

Table 3 Specificity, sensitivity, accuracy and AUC values obtained from classification procedure

	Specificity (%)	Sensitivity (%)	Accuracy (%)	AUC
RT	75	77.5	76.47	0.86
Rip-II	35.71	90	67.65	0.69
OrtRip-II	25	87.5	61.76	0.63
Complex OrtRip-II (imaginary)	75	90	83.82	0.91
Complex OrtRip-II (real)	78.57	87.5	83.82	0.91
Complex OrtRip-II (magnitude)	78.57	90	85.3	0.92
Dual Combined	96.43	95	95.6	0.98
Triple Combined	96.43	97.5	97.06	0.99

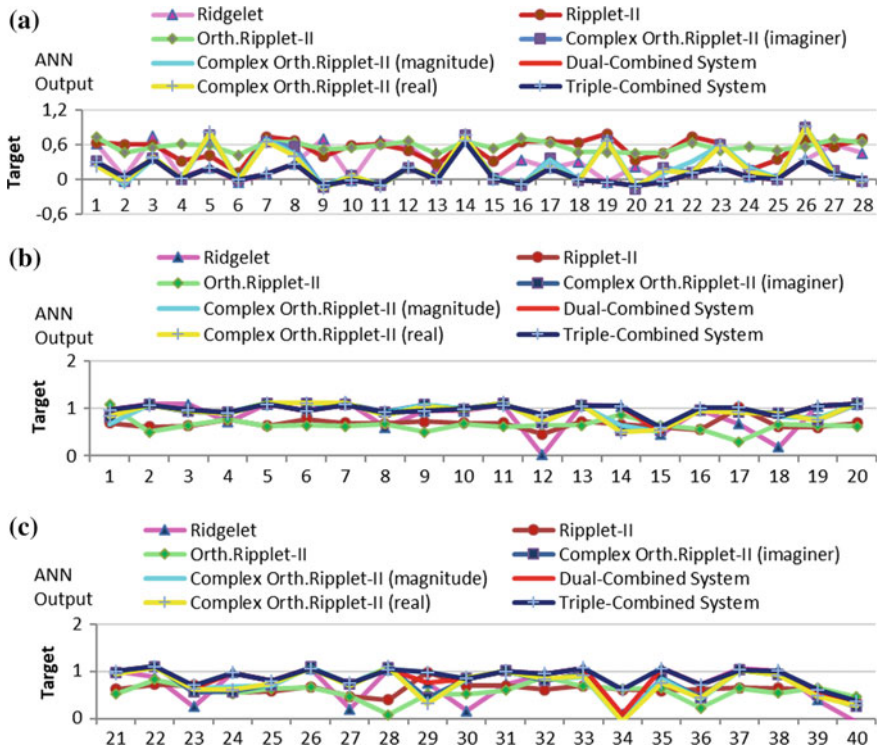

Fig. 10 The results for each image at ANN output: **a** Results of hemangioma images, **b** results of the cyst images (No: 1–20), **c** results of cyst images (No: 21–40)

imaginary parts and magnitude values for complex OrtRip-II) and combined systems are presented in Fig. 11. Calculated AUC values are transferred to Table 3. The systems with an AUC value closer to 1 yield more accurate classification results.

Table 4 Literature on the classification of liver lesions

Study	Methods	Classes	Accuracy (%)	*Spe.* (%)	*Sen.* (%)	AUC
Mojsilovic et al. [16]	Wavelet	Normal, cirrhosis	92.00	–	–	–
Lee et al. [13]	Bayes classifier	Hepatoma, cirrhosis, normal	65.57–97.69	–	–	–
Mala and Sadasivam [14]	Wavelet, neural network	Fatty, cirrhosis	95.00	94.00	96.00	–
Balasubramanian et al. [2]	BPN network, k-means clustering	Normal, cyst, benign, metastases	70.00–93.50	–	–	–
Sela et al. [23]	k-nn classifier, SVM	Healthy, fibrosis, cirrhosis	82.30	–	25.00–100.00	0.700–0.990
Ribeiro et al. [20]	k-nn classifier, SVM	Normal, hepatitis, cirrhosis	59.26–100.00	–	22.22–100.00	–
Hashem et al. [10]	ANN, DT, MLRA, kNN classifiers	Fibrosis degree	80.77–93.55	50.00–100.00	80.00–94.10	0.755–0.971
Jeon et al. [11]	SVM	Cyst, hemangioma, malignancy	59.33–96.50	–	–	–
Singh et al. [26]	Linear classifier	Fatty, normal	95.00	90.00	100.00	
Öztürk and Ceylan [18]	Wavelet, Curvelet, Tetrolet, ANN	Benign, malign	90.00	57.89	87.76	–
Akın and Ceylan [1]	ANN, ELM, Wavelet, complex Wavelet	Hemangioma, cyst	70.50	75.00	64.20	–
Yaşar and Ceylan [31]	Complex Rip-II	Hemangioma, cyst	–	–	–	0.695
In our study (2017)	RT, real and complex OrtRip-II, triple-combined ANN	Hemangioma, cyst	97.06	96.43	97.5	0.990

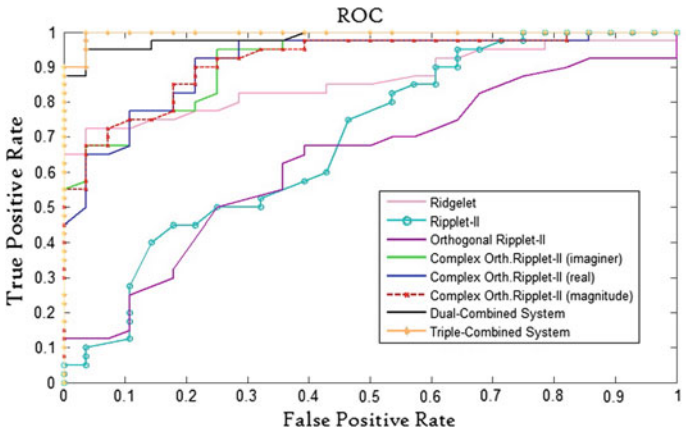

Fig. 11 The ROC curves belong to classification results

5 Conclusion

Complex OrtRip-II, an improved version of Rip-II and OrtRip-II, is proposed in this study. The results of this study prove that the complex OrtRip-II is superior to Rip-II and OrtRip-II as it contains phase information. Considering that the complex OrtRip-II has only recently been developed and used in biomedical classification for the first time, it is clear that the success of the method can be improved using more advanced systems.

This is the first study which uses Rip-II, OrtRip-II and complex OrtRip-II for feature extraction from medical images and compares the results of them in classification applications.

All three methods are based on GRAT; however, they differ in terms of the WT used in their algorithms. While Rip-II is performed with 1D real WT and OrtRip-II is performed with 2D real WT, complex OrtRip-II is performed by using 2D complex WT. The fact that the OrtRip-II which uses 2D real WT gives the worst result among all the methods, while the complex OrtRip-II containing 2D complex WT gives the highest accuracy results among the relevant MRA methods, is proof of the need for the complex form of Rip-II. In this study, Rip-II types have been given a complex form and their performances improved with the combined structure.

When feature extraction is performed using the complex OrtRip-II, the coefficients obtained from the transform are not directly used in the complex form. Instead, real/imaginary components and magnitude values are used separately. The reason for this is that the other MRA methods produce real values and conventional ANN models use real valued data for classification task.

Complex OrtRip-II analysis can be used in different data sets and in different image processing applications. This chapter is a basis for future image processing

applications using complex OrtRip-II., and shows that this transform can be effectively used for feature extraction applications. Comparisons with recent similar applications in the literature reveal that this study makes an important contribution to the classification of liver MR images with a high accuracy ratio.

However, this study was realized using only liver MR images. So, this method may not have such a high performance rate with other medical data sets. The authors plan to carry out various image processing applications to compare the performance of the complex forms of different MRA techniques with complex OrtRip-II by expanding the dataset with different kinds of medical image.

Acknowledgements This study is supported by the Scientific and Technical Research Council of Turkey (TUBITAK, Project No: 113E184).

References

1. Akın M, Ceylan M (2015) Comparison of artificial neural network and extreme learning machine in benign liver lesions classification. Medical technologies national conference (TIPTEKNO), Bodrum, Turkey (in Turkish)
2. Balasubramanian D, Srinivasan P, Gurupatham R (2007) Automatic classification of focal lesions in ultrasound liver images using principal component analysis and neural networks. 29th Conference of IEEE EMBS
3. Beylkin G, Coifman R, Rokhlin V (1991) Fast wavelet transform and numerical algorithms. Commun Pure Appl Math 44:141–183
4. Candes EJ, Donoho DL (1999) Ridgelets: a key to high-dimensional intermittency. Philos Trans Royal Soc London A 357:2495–2509
5. Ceylan M, Özbay Y, Uçan ON, Yıldırım E (2010) A novel method for lung segmentation on chest CT images: complex-valued artificial neural network with complex wavelet transform. Turk. J Electr Eng Comput Sci 18:613–624
6. Chen GY, Bui TD, Krzyzak A (2005) Rotation invariant pattern recognition using ridgelets, wavelet cycle-spinning and Fourier features. Pattern Recogn 38:2314–2322
7. Chen GY, Kegl B (2007) Image denoising with complex ridgelets. Pattern Recogn 40:578–585
8. Do MN, Vetterli M (2003) The finite ridgelet transform for image representation. IEEE Trans Image Process 12:16–28
9. Eiber M, Fingerle AA, Brügel M, Gaa J, Rummeny EJ, Holzapfel K (2012) Detection and classification of focal liver lesions in patients with colorectal cancer: retrospective comparison of diffusion-weighted MR imaging and multi-slice CT. Eur J Radiol 81:683–691
10. Hashem AM, Rasmy ME, Wahba KM, Shaker OG (2012) Single stage and multistage classification models for the prediction of liver fibrosis degree in patients with chronic hepatitis C infection. Comput Methods Programs Biomed 105:194–209
11. Jeon JH, Choi JY, Lee S, Ro YM (2013) Multiple ROI selection based focal liver lesion classification in ultrasound images. Expert Syst Appl 40:450–457
12. Lawton W (1993) Applications of complex valued wavelet transforms to subband decomposition. IEEE Trans Sig Process 41:3566–3568
13. Lee WL, Chen YL, Hsieh KS (2003) Ultrasonic liver tissues classification by fractal feature vector based on M-band wavelet transform. IEEE Trans Med Imaging 22:382–392
14. Mala K, Sadasivam V (2005) Automatic segmentation and classification of diffused liver diseases using wavelet based texture analysis and neural network. IEEE INDICON conference, Chennai, India

15. Mitrea D, Nedevschi S, Lupsar M, Socaciv M, Badea R (2010) Experimenting various classification techniques for improving the automatic diagnosis of the malignant liver tumors, based on ultrasound images, 3rd International congress on image and signal process, Yantai, China
16. Mojsilovic A, Popovic M, Sevic D (1996) Classification of the ultrasound liver images with the 2N X 1-D wavelet transform. IEEE international conference on image process, Lausanne, Switzerland
17. Öztürk AE (2015) Detecting the liver focal lesions by using ripplet, tetrolet and ridgelet transforms. MS Thesis, The graduate school of natural and applied science of Selcuk University, Konya, Turkey (in Turkish)
18. Öztürk AE, Ceylan M (2015) Fusion and ANN based classification of liver focal lesions using phases in magnetic resonance images. International symposium on biomedical imaging (ISBI), New York, USA
19. Öztürk AE, Ceylan M (2016) A new transform for medical image denoising: Fused tetrolet transform. J Med Imaging Health Inform 6:358–366
20. Riberio R, Marinho RT, Velosa J, Ramalho F, Sanches JM, Suri JS (2011) The usefulness of ultrasound in the classification of chronic liver disease. 33rd Annual International Conference of IEEE EMBS, Boston, USA
21. Saba L, Dey N, Ashour AS, Samanta S, Nath SS, Chakraborty S, Sanches J, Kumar D, Marinho RT, Suri JS (2016) Automated stratification of liver disease in ultrasound: an online accurate feature classification paradigm. Comp Methods Prog Biomed 130:118–134
22. Sathesh Manoharan S (2010) A dual tree complex wavelet transform construction and its application to image denoising. Int J Image Process 3:293–300
23. Sela Y, Freiman M, Dery E, Edrei Y, Safadi R, Pappo O (2011) fMRI-Based hierarchical SVM model for the classification and grading of liver fibrosis. IEEE Trans Biomed Eng 58:2574–2581
24. Selesnick IW, Baraniuk RG, Kingsbury NG (2005) The dual-tree complex wavelet transform. IEEE Sig Process Mag 22:123–151
25. Singh M, Singh S, Gupta S (2011) A new measure of echogenicity of ultrasound images for liver classification. 24th Canadian conference electrical and computer engineering, Niagara Falls, USA
26. Singh M, Singh S, Gupta S (2014) An information fusion based method for liver classification using texture analysis of ultrasound images. Inf Fusion 19:91–96
27. Suganya R, Rajaram S (2012) Classification of liver diseases from ultrasound images using a hybrid kohonen SOM and LPND speckle reduction method. IEEE International Conference Signal Process. Computer and Control, Waknaghat Solan, India
28. Unser M (1995) Texture classification and segmentation using wavelet frames. IEEE Trans Image Process 4:1549–1560
29. Wang X (2010) Moving window pyramid-based ridgelet transform for image denoising. International conference on audio language and image process, pp 1710–1713, Shanghai, China
30. Xu J, Wu D (2012) Ripplet-II transform for feature extraction. IET Image Process 6:374–385
31. Yaşar H, Ceylan M (2016) A new method for extraction of image's features: complex discrete Ripplet-II transform. Sig Process Comm Appl Conf, Zonguldak, Turkey (in Turkish)
32. Yaşar H, Ceylan M, Öztürk AE (2013) Comparison of real and complex-valued versions of wavelet transform, curvelet transform and ridgelet transform for medical image denoising. IJEMME 3:427–436

http://www.springer.com/978-3-319-65980-0

Classification in BioApps
Automation of Decision Making
Dey, N.; Ashour, A.; Borra, S. (Eds.)
2018, XIII, 447 p. 228 illus., 123 illus. in color.,
Hardcover
ISBN: 978-3-319-65980-0